Ideal MHD Stability of $m \geq 2$ Modes in Diffuse High-β, $\ell = 1$ Equilibria

F. Herrnegger, W. Schneider

IPP 1/161 June 1976

MAX-PLANCK-INSTITUT FÜR PLASMAPHYSIK

8046 GARCHING BEI MÜNCHEN

MAX-PLANCK-INSTITUT FÜR PLASMAPHYSIK

GARCHING BEI MÜNCHEN

Ideal MHD Stability of $m \geq 2$ Modes in Diffuse High-β, $\ell = 1$ Equilibria

F. Herrnegger, W. Schneider

IPP 1/161 June 1976

Die nachstehende Arbeit wurde im Rahmen des Vertrages zwischen dem Max-Planck-Institut für Plasmaphysik und der Europäischen Atomgemeinschaft über die Zusammenarbeit auf dem Gebiete der Plasmaphysik durchgeführt.

IPP 1/161

F. Herrnegger
W. Schneider

Ideal MHD Stability of $m \geq 2$ Modes in Diffuse High-β, $\ell = 1$ Equilibria

June 1976 (English)

Abstract

A time-dependent explicit finite difference code is developed for computing growth rates of gross magneto-hydrodynamic modes in helically symmetric high-β, $\ell = 1$ equilibria. The effect of numerical dispersion on current-driven and pressure-driven modes and the convergence of the growth rate with the grid size for modes in screw-pinch, θ-pinch, and helical equilibria are discussed. In the case of diffuse MHD equilibria with a long helical period length, the eigenvalues computed by this code are in agreement with those of a δW-analysis and of experiments and are a factor of about two smaller than the surface current theory predicts. The growth rates of $m \geq 2$ modes are given as functions of the helical period number, the helical amplitude of the magnetic axis, beta, and the longitudinal wave number k.

INDEX

1. Introduction

The investigation of the linear magnetohydrodynamic (MHD) stability of helically symmetric high-β equilibria with diffuse pressure profile and a spatial magnetic axis is of considerable significance for the toroidal high-β experiments Isar T1 /1/, Scyllac /2/, and the HBS II /3/. In leading order, the stability of these toroidal equilibria of large aspect ratio and with many periods around the torus is determined by the stability properties of helically symmetric equilibria.

In the past, several approximating assumptions about the ordering /4, 5, 6/ and the pressure profile have been used to calculate the growth rate of unstable modes in these systems /2/. One important result of the stability theory based on the old Scyllac ordering /4, 5/ and using a constant pressure model is that the $m = 1$, $k = 0$ mode can be wall-stabilized for a sufficiently small compression ratio (b/a) by the dipole currents induced in the conducting wall. For a diffuse pressure profile and using the same old ordering, there are, besides the gross $m = 1$ mode, two additional classes of rather localized $m = 1$ modes /7/. One set of modes existing for every monotonic pressure profile is localized in the interior of the plasma and cannot be wall-stabilized, while the other set of modes is localized rather in the exterior of the dense plasma and can be wall-stabilized. However, the growth rates of these modes are a factor of the order ε ($\varepsilon = ha$, a being the mean plasma radius, $L = 2\pi/h$ the period length of the $\ell = 1$ field) smaller than the gross $m = 1$ mode in the case of no wall stabilization. The corresponding growth time is typically about $50\mu s$ and hence up to now these modes have not been observed hitherto in experiments. Hence we will not deal further with $m = 1$ modes which have no implication in a wall-stabilized experiment during a time scale of interest, but investigate instead the $m = 2$ modes growing in a shorter time scale. There are some theoretical and experimental facts discussed below which called for the investigation of $m = 2$ instabilities in helical configurations of small compression ratio.

According to the surface current theory /4, 5/, the MHD growth rate of the $m = 2$, $k = 0$ mode for typical plasma parameters is a factor of the order $\mathcal{O}(\sqrt{m(m-1)}/ha)$ as large as that of the $m = 1$, $k = 0$ mode in the case of no wall stabilization. However,

the experimental results /1/ indicate that the m = 2 mode cannot be observed or, if it is observed as in the collision-dominated regime, the growth rate is less than the surface current theory predicts. This fact was a strong motivation for developing a model to study the effect of a diffuse profile on the reduction of the growth rate of $m \geq 2$ modes.

More recently, Herrnegger and Nührenberg /8/ studied the stability of toroidal high-β, $\ell = 1$ equilibria with a diffuse pressure profile and a vacuum field outside with respect to localized modes by means of general stability criteria. They showed that (a) for sufficiently high β-values ($\beta \gtrsim 0.75$) and a compression ratio of about 2, the Mercier criterion is satisfied almost everywhere except in a very narrow region around the magnetic axis, (b) a mean high-β magnetic well exists for β-values of $\beta \gtrsim 0.23$ and (c) the vacuum magnetic field between plasma and wall has a magnetic well, too; hence the plasma is surrounded by a region of increasing mean value of $\overset{o}{B}^2$. These results have been an additional motivation for studying the stability behaviour of helical equilibria without using any expansions.

Very recently, Marder /9/ investigated the m = 2,3 modes for a helically symmetric diffuse pressure profile by means of a δW-analysis using the new Scyllac ordering, which does not include terms of order ε. However, in the present code, we do not make any restricting assumptions about ordering and pressure profile but include all physical properties of helically symmetric MHD equilibria. The stabilizing effect of ion gyro-motion on the m = 2 modes /10, 11/ can be implemented into the code but we do not deal with this effect at present.

There are essentially two distinct approaches to solving the linearized stability problem. The variational approaches utilize the Lagrangian to formulate an eigenvalue problem /12/. The solution is found by using the Rayleigh-Ritz /13/ or the Galerkin /12/ procedures where either global expansion functions /14/ or finite elements /12, 15, 16/ are taken as a basis. An efficient approach is a combination /12/ of finite elements to represent variation normal to the magnetic surfaces and Fourier series for behaviour in them.

The other major technique which we are using is to treat the initial-boundary-value problem /17, 18/, where the evolution of linearized perturbations is followed in time. The unstable mode with the largest growth rate will separate from the others after some time. As we shall show below, rather small growth rates can be calculated. This method allows the investigation of nonlinear ideal /19, 20/ and non-ideal MHD effects /21 - 23/ to be implemented in a straightforward manner in problems depending on two space variables and the treatment of three-dimensional nonlinear problems /24 - 27/.

The method of solution is essentially the same as that developed by Bateman-Schneider-Grossmann /18/ to investigate the stability of belt-pinch equilibria. In contrast to the belt-pinch-type equilibria, however, the instabilities in the high-β stellarator configuration (HBS) without longitudinal net current are not current-driven modes but pressure-driven modes and have a very small nondimensional growth rate. Therefore, the computational effort has to be considerably increased for calculating these small growth rates.

In Sec. 2 the linearized ideal MHD equations formulated in a helical coordinate system and the boundary conditions are given. Section 3 describes the numerial solution of the initial-boundary-value problem and the calculation of the eigenvalues. The numerical dispersion and dissipation is systematically investigated for current-driven and pressure-driven modes in screw-pinch, θ-pinch, and helically symmetric high-β equilibria. In Section 4, the eigenfunctions and the eigenvalues of $m = 2, 3$ modes as functions of the helical distortion, the longitudinal wave number k, and β are given for a particular ha.

2. The Model

We perform a numerical mode analysis of global MHD modes in a configuration where the plasma touches the wall; hence there is no vacuum region between plasma and wall. The basic equations for the model /28, 29/ are the ideal MHD equations. These equations are linearized about a given helically symmetric, and hence two-dimensional, equilibrium; we then Fourier-analyze these equations along the ignorable coordinate and get a system of partial differential equations depending on time and on two dimensions of space. All perturbed quantities are complex functions in order to describe the phase of the Fourier components. Together with appropriate initial values and boundary conditions, this initial-boundary-value problem is solved numerically using an explicit difference scheme. The results of this computation are the eigenfunctions $\vec{v}$, p, and $\vec{B}$, and the associated eigenvalues, i.e. the growth rates.

This is the general survey of the method; i.e. how the instabilities of helically symmetric equilibria are calculated.

The ideal MHD equations from which we start are given in nonlinear form

$$\frac{\partial}{\partial t}\rho + \nabla\cdot(\rho\,\vec{v}) = 0, \tag{1}$$

$$\rho\left(\frac{\partial}{\partial t} + \vec{v}\cdot\nabla\right)\vec{v} + \nabla p - \vec{J}\times\vec{B} = 0, \tag{2}$$

$$\frac{\partial}{\partial t}p + \nabla\cdot(p\,\vec{v}) + (\varkappa - 1)\,p\,(\nabla\cdot\vec{v}) = 0, \tag{3}$$

$$\frac{\partial}{\partial t}\vec{B} + \nabla\times\vec{E} = 0, \tag{4}$$

$$\mu_0\vec{J} = \nabla\times\vec{B}, \tag{5}$$

$$\vec{E} + \vec{v}\times\vec{B} = o \tag{6}$$

where ρ is the mass density, $\vec{v}$ is the flow velocity, p is the pressure, $\vec{B}$ is the magnetic field, and μ_o is the magnetic permeability of the vacuum. Equation (3) describes an adiabatic change of state, where $\varkappa = c_p/c_v$ is the ratio of specific

heats, which we usually specify as $\chi = 5/3$. The current density $\vec{J}$ and the electric field $\vec{E}$ are determined from Ampere's law and Ohm's law, respectively. Equation (1) for the mass density is not needed since the change of pressure p appearing in the equation of motion is determined by Eq. (3).

2.1 Coordinate System and Equilibrium

The coordinate system in which the initial-boundary-value problem is solved, and in which the helical equilibria are calculated, is a non-orthogonal helical coordinate system (x^1, x^2, x^3). This system (see Fig. 1) consists of cartesian coordinates (x^1, x^2) rotating around the straight z-axis; the period length $L = 2\pi/h$ along z is the period length of the $\ell = 1$ field. The coordinate transformations and the metric tensor are given in App. A.

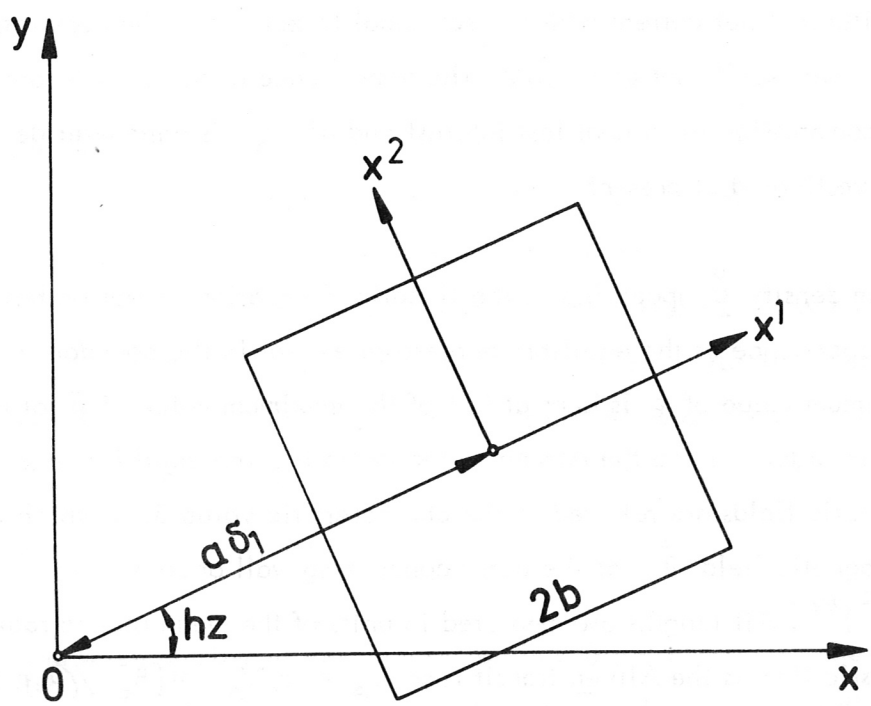

Fig. 1: Helical coordinate system (x^1, x^2, x^3) with the origin at 0.

The magnetic field $\overset{\circ}{\vec{B}}$ and the current density $\overset{\circ}{\vec{J}}$ of diffuse, helically symmetric high-β, $\ell = 1$ MHD equilibria which are independent of x^3, are given in App. A in terms of its covariant and contravariant components. The solution is computed numerically for a special choice of the equilibrium pressure function $\overset{\circ}{p} = \overset{\circ}{p}(\psi)$ and of the second free function $I(\psi)$, as is described in App. A.
The equilibrium has the special property that the longitudinal net current vanishes on each magnetic surface ($J_c = 0$). The outermost magnetic surface of these equilibria is a square of side length 2b which coincides with coordinate surfaces, and which has a helical displacement $D_1 = a\delta_1$ from the coordinate axis. This is numerically the simplest boundary curve where we can put the boundary conditions for the disturbances and the equilibrium quantities. Some examples of helical equilibria are given in Appendix A (see Fig. 14).

The five dimensionless parameters of these equilibria are the helical displacement δ_1, the period number $\varepsilon = ha$, $\beta = \overset{\circ}{p} / (\overset{\circ}{\vec{B}}^2 / 2\mu_0 + \overset{\circ}{p})$ at the magnetic axis, J_c characterizing the longitudinal net current which is set equal to zero, and the compression ratio b/a which we usually set equal to 2. The dependence of the growth rate of m = 2 modes on the compression ratio is of less interest and hence this parameter dependence is not being investigated at present.

The equilibrium density $\overset{\circ}{\rho}$ appearing in the linearized equation of motion has the same spatial dependence as the equilibrium pressure except in the boundary region where the minimum value of $\overset{\circ}{\rho}$ is kept at 0.1 of the maximum value of $\overset{\circ}{\rho}$ at the magnetic axis in order to keep the Alfvèn velocity finite. The equilibrium and the perturbed magnetic fields are referred to the characteristic value B_c, which is related to the magnetic field $\vec{B}_0$ at the outer conducting wall according to $B_c = (g_{33}\, \vec{B}_0^{\,2})^{1/2}$. All lengths are measured in units of the mean plasma radius a. The characteristic time is the Alfvèn transit time $\tau_A = a/V_A = [B_c^2 / (\mu_0 \rho_0 a^2)]^{-1/2}$, where the equilibrium mass density ρ_0 is taken at the magnetic axis. From this normalization it follows that the growth rate γ computed by the code is related to the dimensional growth rate $\hat{\gamma}$ as $\gamma = \hat{\gamma}\, \tau_A$.

Because the square boundary rotates, all these equilibria we use at present have a small $\ell = 4$ field component which entails a destabilizing effect. According to the surface current model, however, the relative change of the growth rate of $m = 2$ modes due to this δ_4 -distortion, which is typically $\delta_4 \simeq 0.03$, is negligible.

2.2 Linearization and Fourier Analysis of the Initial-Boundary-Value Problem

We linearize the Eqs. (2) - (6) around a given static MHD equilibrium solution represented by the functions $\overset{0}{p}$, $\overset{0}{\vec{B}}$ and which is described in the previous section: $Q = \overset{0}{Q} + \varepsilon \overset{1}{Q}$. In addition, we drop the index 1 at the perturbed quantities; ε is the arbitrary small perturbation parameter. The perturbed state is completely represented by the seven functions $\vec{v}$, p, $\vec{B}$. Since the equilibrium solution is independent of x^3 and hence the coefficients of this linearized system of differential equations do not depend on x^3 , we can make a Fourier analysis along this ignorable coordinate x^3 :

$$Q(x^1, x^2, x^3, t) = \tilde{Q}(x^1, x^2, t) \exp(iK x^3),$$

where all perturbed quantities $\tilde{Q}$ are complex functions ($i = \sqrt{-1}$). The imaginary part of the complex solution describes the physical quantities at a plane $x^3 = \lambda/4$ displaced a quarter-wave length of the unstable mode in the x^3 -direction ($\lambda = 2\pi/K$). We also drop the tilde and have to investigate each Fourier component Q for a given wave number K of the mode. Because the (x^1, x^2)-plane rotates around x^3 , the wave number K in the rotating coordinate system is associated with a set of (k, m)-modes in a frame at rest according to

$$k = -K - mh. \qquad (7)$$

Here, k is the wave number in the z-direction in a frame at rest and the azimuthal mode number m gives the number of vortex pairs of $\vec{v}$ in the azimuthal direction. After doing this and keeping in mind that all perturbed quantities are complex, we get the following system of partial differential equations for the contravariant components of the perturbed velocity v^i and magnetic field B^i , and the perturbed pressure p:

$$\mathring{\rho}\frac{\partial}{\partial t}v^i + g^{i\ell}\left\{ p_{,\ell} - \sqrt{g}\,\varepsilon_{jk\ell}\,(J^j \mathring{B}^k + \mathring{J}^j B^k)\right\} = 0, \tag{8}$$

$$\frac{\partial}{\partial t}p + v^i \mathring{p}_{,i} + \varkappa \mathring{p}\,\frac{1}{\sqrt{g}}(\sqrt{g}\,v^i)_{,i} = 0, \tag{9}$$

$$\frac{\partial}{\partial t}B^k + \frac{1}{\sqrt{g}}\varepsilon^{ijk}E_{j,i} = 0, \tag{10}$$

$$E_k = -\sqrt{g}\,\varepsilon_{ijk}\,v^i \mathring{B}^j, \qquad J^k = \frac{1}{\sqrt{g}}\varepsilon^{ijk}B_{j,i}. \tag{11}$$

For brevity, derivatives are denoted by indices $,j := \partial/\partial x^j$ and the usual summation convention is used; here the derivation $\partial/\partial x^3$ has to be substituted by iK. The permutation symbols are denoted by ε_{ijk} and ε^{ijk}. In App. B, the system (8) - (11) is given in component form. This hyperbolic system of first order in time and two-dimensional in space was solved numerically together with the boundary conditions for an electrically conducting wall at a square boundary of side length 2b (see Sec. 2.1):

$p = 0$ (12), $\qquad \vec{n}\cdot(\vec{E}_{(a)} - \vec{E}_{(i)}) = 0$ (13), $\qquad \vec{n}\times\vec{E} = 0$ (14),

where $\vec{n}$ is the unit vector normal to the boundary and is simply related to the covariant base vectors $\vec{e}^i$. The condition (13) is for numerical reasons only and defines the normal component of the electric field $\vec{E}_{(a)}$ at the artificial points outside the conducting boundary in terms of the electric field $\vec{E}_{(i)}$ at the interior points next to the boundary. This condition states that the electric surface charge, which cannot be prescribed by the boundary conditions, is determined by the differential equations. The analytic equivalent form of $(\vec{n}\cdot\vec{v}) = 0$ was not used for numerical reasons. A suitable choice of initial values immaterial to the solution of the eigenvalue problem is described in Sec. 3.1.

3. Numerical Solution

In this section we shall describe the numerical method of solution; in particular we discuss the effort to get reliable results by this code.

3.1 Solution of the Initial-Boundary-Value Problem

Difference Scheme:

The difference approximation was made in a grid staggered in space and time: at a given time step in the numerical calculation, the various physical quantities are staggered over the mesh.

On the o-grid, the physical boundary curve, the perturbed pressure p and the perturbed magnetic field $\vec{B}$ are defined; on the + - grid, the equilibrium quantities, the perturbed current density $\vec{J}$ and the electric field $\vec{E}$ are defined. This layout helps the space and time centering of the various difference equations. The grid size Δx is the same in the x^1 and x^2 -directions. The difference approximation used here is of second-order accuracy. More details concerning the grid are given in Appendix C.

For the explicit difference scheme that we use, the maximum time step permitted by numerical stability considerations is determined by the maximum magnetoacoustic velocity V_M of the equilibrium solution:

$$\Delta t \leq \Delta x / V_M \,. \tag{15}$$

An advantage of the linearized system is that this maximum time step is constant during a run. In general, we used 0.8 of the maximum value.

Symmetry Properties:

The equilibrium solution $\psi(x^1, x^2)$ is symmetric with respect to the osculating plane of the magnetic axis and therefore is an even function of x^2, $\psi(x^1, x^2) = \psi(x^1, -x^2)$, hence the magnetic field and the current density of the equilibrium have the following symmetry properties: the $\overset{\circ}{B}{}^1$, $\overset{\circ}{B}_1$, $\overset{\circ}{J}{}^1$, $\overset{\circ}{J}_1$ components are odd functions of x^2, all other components of $\overset{\circ}{\vec{B}}$ and $\overset{\circ}{\vec{J}}$ are even functions of x^2.

Therefore the complex solution of Eqs. (8) - (11) have the following symmetry properties with respect to x^2:

$$B^1(x^1, x^2) = -B^{1*}(x^1, -x^2), \qquad v^1(x^1, x^2) = v^{1*}(x^1, -x^2),$$

$$B^2(x^1, x^2) = B^{2*}(x^1, -x^2), \qquad v^2(x^1, x^2) = -v^{2*}(x^1, -x^2),$$

$$B^3(x^1, x^2) = B^{3*}(x^1, -x^2), \qquad v^3(x^1, x^2) = -v^{3*}(x^1, -x^2),$$

$$J^1(x^1, x^2) = -J^{1*}(x^1, -x^2), \qquad p(x^1, x^2) = p^*(x^1, -x^2),$$

$$J^2(x^1, x^2) = J^{2*}(x^1, -x^2),$$

$$J^3(x^1, x^2) = J^{3*}(x^1, -x^2),$$

where * denotes the complex conjugate value. Starting with initial values of the perturbed quantities obeying these symmetry conditions, the computation can be performed on half of the (x^1, x^2) plane only because the difference approximation conserves these properties.

Initial Values:

The solution of the eigenvalue problem treated as initial-boundary-value problem must not depend on the initial values of the perturbed quantities. Hence any arbitrary function can be used as initial values for the velocity field (or the pressure or the magnetic field, which has to be devergence-free) which are not completely orthogonal to the unstable modes of interest in the parameter range. However, in order to save computing time, we start with a specific velocity distribution roughly resembling the particular mode and having some characteristic properties of the eigenfunctions, namely divergence-free in lowest order of δ_1 for transverse modes ($k = 0$) and a $\cos(m\varphi)$ - dependence on the azimuthal angle φ. An example of such a velocity field, represented in a polar coordinate system (r, φ) with the origin at D_1, is given below:

$$v_r = f_r \exp[-im(\varphi - \alpha)], \quad v_\varphi = -i f_\varphi \exp[-im(\varphi - \alpha)], \quad v^3 = 0. \tag{16}$$

The functions f_r, f_φ are specified for different m-numbers as follows ($R = \pi r/r_o$):

$m = 0$: $f_r = A \sin R$, $f_\varphi = -A \sin R$;

$m = 1$: $f_r = (A/R) \sin R$, $f_\varphi = A \cos R$;

$m = 2, 3, \ldots$: $f_r = A \sin R$, $f_\varphi = (A/m)(\sin R + R \cos R)$.

From these the velocity components v^1 , v^2 are calculated by using the transformations between cylindrical and cartesian vector components. Within the circle $r = r_0$ the perturbations are excited, the amplitude and the phase of which are denoted by A and α , respectively. All other perturbed quantities are initially set equal to zero.

We learned that, by using velocity fields with vanishing divergence ($\nabla \cdot \vec{v} = 0$) initially, the amplitudes of high-frequency compressional oscillations are considerably reduced.

As an alternative to the above described initial conditions, we use as initial values the eigenfunctions of a previous run for similar parameters.

3.2 Calculation of Eigenfunctions and Eigenvalues

The posed initial-boundary-value problem, Eqs. (8) - (14), is solved by the explicit difference method described above. After some e-folding times, the most unstable mode in the system overwhelms all other motion and the resulting spatial functions $\vec{v}$, p , and $\vec{B}$ are the eigenfunctions for the given parameters. The calculation is carried on till these functions obey the relation

$$Q\,(x^1, x^2, t) = \hat{Q}\,(x^1, x^2)\,\exp(\gamma t)\,,$$

where Q is any perturbed quantity and the eigenfunction $\hat{Q}\,(x^1, x^2)$ remains constant in time.

The physical high-frequency oscillations in the system can be damped very quickly by averaging all functions in time at each grid point and taking these new values as new initial values.

The growth rate γ can be calculated at every grid point by

$$\gamma = \frac{\partial}{\partial t} \ln v^1 \,. \qquad (17)$$

But normally there is much noise particularly in the region of low density near the wall. Therefore we either use the spatial integral of the kinetic energy

$$\bar{E}_{kin.}(t) = \iint \tfrac{1}{2} \overset{o}{\rho} (\mathrm{Re}\,\vec{v})^2 \, dx^1 \, dx^2 \,, \quad Y_E(t) = \bar{E}_{kin.}^{1/2} \,, \tag{18}$$

or the spatial integral of the perturbed pressure or of the radial velocity multiplied by a weight function /28/:

$$Y_p(t) = \iint p \cos(m\varphi) \, dx^1 \, dx^2 \,, \tag{19}$$

$$Y_v(t) = \iint v_r \sin(m\varphi) \, dx^1 \, dx^2 \,. \tag{20}$$

For the natural logarithm of these functions Y (t), a least squares fit is made to obtain the growth rate γ .

3.3 Numerical Convergence

Before using this code for investigating the stability behaviour of helical $\ell = 1$ equilibria, we performed several reliability tests. In particular, we investigated the convergence properties of the numerical scheme, i.e. we calculated the eigenvalues of different modes in different configurations as functions of the grid size Δx. We started the investigation with current-driven modes. In addition, we checked to see whether the code guarantees linear superposition of different modes. We excited simultaneously as well as successively m = 1 and m = 2 modes of equal initial amplitude, run the calculation a characteristic time, and finally added the eigenfunctions of the m = 1 and m = 2 calculations. The result of this second run was identical with the first, where the two modes had been simultaneously excited.

3.3.1 Screw-pinch

The first application of the model described above, is a screw-pinch equilibrium with straight magnetic axis and a superimposed $\ell = 4$ field. The longitudinal current is fairly large so that current-driven instabilities with relatively large growth rates are expected.

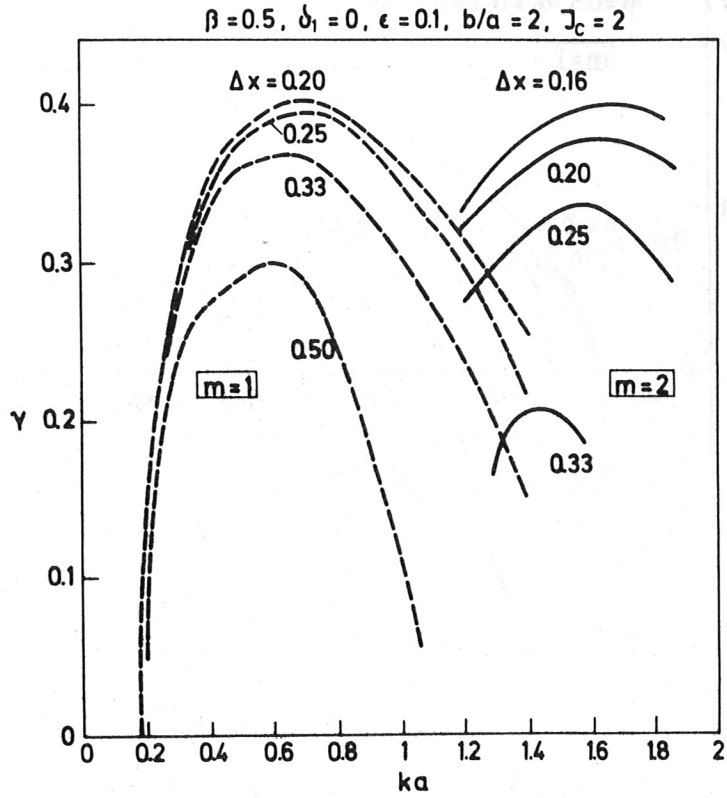

Fig. 2: Dispersion curve γ *vs* ka of m = 1 (---) and m = 2 (——) modes in a screw pinch for various grid sizes Δx.

In Fig. 2, the dependence of the growth rate on the grid size Δx versus wave number k of m = 1, 2 modes is shown. For the m = 1 mode sufficient accuracy is obtained for a moderate number of mesh points, i.e. the 24x24 ($\Delta x = 1/6$) grid yields results within an accuracy of approximately 10%. The convergence of the m = 2 mode is worse, which is qualitatively understandable because of the finer structure of the mode. In the coarser grids, the results are shifted towards stability, which may be due to dissipative effects arising from the difference approximation. The maxima of the dispersion curves are slightly shifted to larger ka values as Δx decreases.

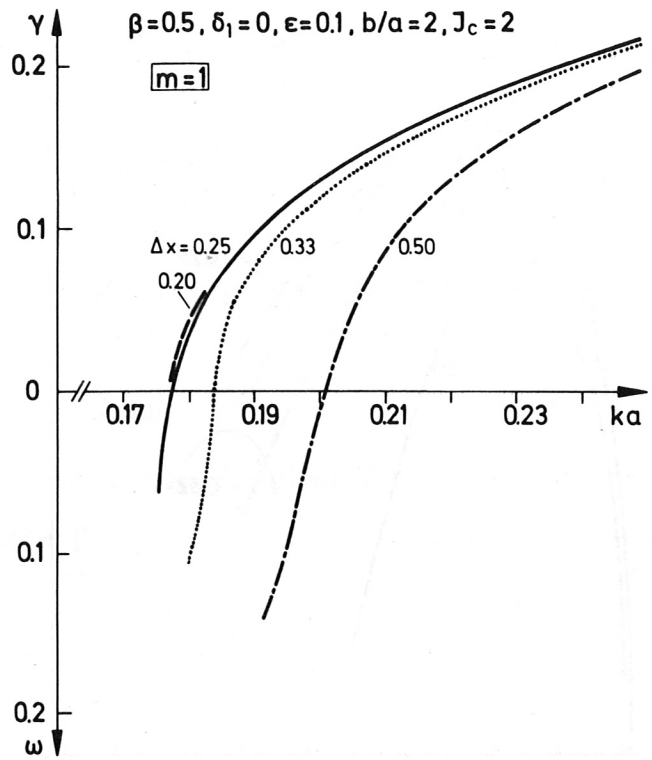

Fig. 3: Dispersive effect of finite grid size near the marginal point.

Another effect directly related to the finite grid size is demonstrated in Fig. 3. This plot shows the dispersion curve γ (ka) of an m = 1 mode near the marginal point for different mesh shizes Δx. The finite difference approximation causes a fairly large shift of the dispersion curve to larger ka values, this being a dispersive effect of the difference approximation.

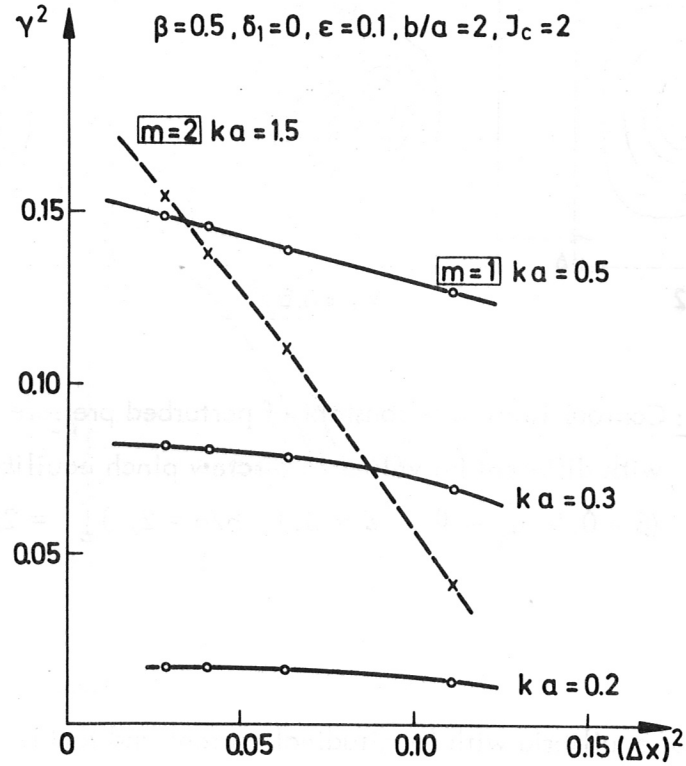

Fig. 4a: Convergence behaviour of eigenvalue γ^2 of m = 1 (——) and m = 2 (---) modes with different ka values in screw-pinch-like equilibria.

In Fig. 4a the different convergence behaviour of various m modes is shown. The solid curves are for m = 1 modes, the first one for ka = 0.5 approximately at the maximum of the dispersion curve. With increasing ka values, the mode becomes more localized, as can be seen from contour plots of the perturbed pressure (Fig. 4b), and hence the slope of the convergence curve increases. The convergence curve of the m = 2, ka = 1.5 mode (this ka value is near the maximum of the dispersion curve) is about a factor of 4 as steep as that for the m = 1 mode, i.e. the convergence of higher m modes is considerably slower than for the m = 1 mode. This fact is plausible because of the finer structure of higher m modes. A roughly second-order convergence of the eigenvalues γ^2 as $(\Delta x)^2$ has been obtained for the current-driven unstable modes in screw-pinch-type equilibria.

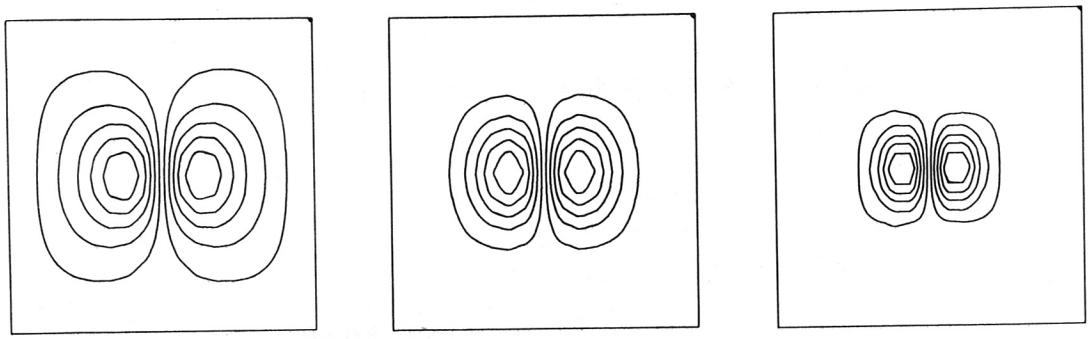

Fig. 4b: Contour lines p = constant of perturbed pressure of m = 1 modes with different ka values in a screw pinch equilibrium ($\beta = 0.5$, $\delta_1 = 0$, $\varepsilon = 0.1$, $b/a = 2$, $J_{/c} = 2$).

3.3.2 θ-Pinch

Leaving this class of equilibria with longitudinal current and tackling the stellarator-type equilibria with vanishing longitudinal net current, the situation gets more difficult. Before using the code for studying the stability of general $\ell = 1$ equilibria, we tested it on the zeroth order approximation of such equilibria, i.e. for $\delta_1 = 0$, and small but finit ε, or, in other words, for the θ-pinch with a superimposed $\ell = 4$ field. The upper curve in Fig. 5 shows the eigenvalue γ^2 vs Δx of an m = 1, ka = 0 mode for $\varepsilon = 0.1$ ($\delta_4 \cong 0.03$). The extrapolated value of γ^2 for $\Delta x \to 0$ gives a real growth rate which is considerably smaller than γ^2_{sc} ($\varepsilon = 0.1$) predicted by the surface current model /4/. Reducing the influence of the $\ell = 4$ field on the instability by increasing the helical period length, one should get in the limit of $\varepsilon \to 0$ marginal stability behaviour, which means $\gamma^2 = 0$; this is illustrated by the dashed curve which is calculated for $\varepsilon = 0.01$.

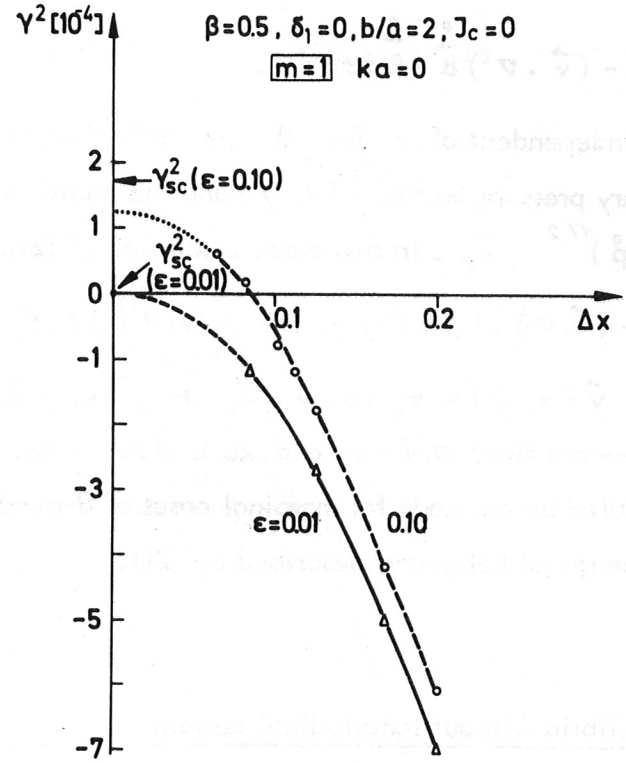

Fig. 5: Eigenvalue γ^2 vs Δx of m = 1, ka = 0 mode in a θ-pinch-like equilibrium with different ε values ($\delta_4 \simeq 0.03$).

In both cases the eigenvalue γ^2 converges as $(\Delta x)^2$. In the case of $\varepsilon = 0.01$, the eigenvalue $\gamma^2 = 0$ extrapolated from the stable side is in accordance with the theoretical marginal value.

The eigenvalue $\gamma^2 = 0$ is highly degenerate. It is easy to show that the linearized unsteady MHD equations (8) - (11) have marginal solutions of the type

$$\vec{v} = \vec{v}(\vec{x}), \quad p = p(\vec{x})\, t, \quad \vec{B} = \vec{B}(\vec{x})\, t \,, \tag{21a}$$

where the velocity is constant in time, and the pressure and magnetic field grow linearly in time. The initial conditions put in Sec. 3.1 are satisfied by the ansatz (21a). The velocity field $\vec{v}$ has to obey the boundary condition $(\vec{v} \cdot \vec{n}) = 0$. The spatial dependence of these solutions is determined by the differential equation for $\vec{v}$:

$$\nabla \left[(\vec{v} \cdot \nabla \mathring{p}) + \varkappa \mathring{p} (\nabla \cdot \vec{v}) \right] - \mathring{\vec{B}} \times (\nabla \times \vec{Q}) + \mathring{\vec{j}} \times \vec{Q} = 0 \tag{21b}$$

where for the moment

$$\vec{Q} := (\vec{\overset{\circ}{B}} \cdot \nabla)\,\vec{v} - (\vec{v} \cdot \nabla)\,\vec{\overset{\circ}{B}} - \vec{\overset{\circ}{B}}\,(\nabla \cdot \vec{v}) .$$

Solutions of (21b) being independent of z ($ka = 0$) are easily found for θ-pinch equilibria with an arbitrary pressure profile $\overset{\circ}{p}(x, y)$ and the equilibrium magnetic field $\vec{\overset{\circ}{B}} = \overset{\circ}{B}_z \vec{e}_z = (1 - 2\overset{\circ}{p})^{1/2} \vec{e}_z$. In this case, a solution of (21b) is given by

$$p(x, y, t) = -(\vec{v} \cdot \nabla \overset{\circ}{p})\,t\,, \quad \vec{B}(x, y, t) = -(\vec{v} \cdot \nabla \overset{\circ}{B}_z)\,t\,\vec{e}_z\,, \tag{21c}$$

where the velocity field $\vec{v}(x, y) = v_x(x, y)\,\vec{e}_x + v_y(x, y)\,\vec{e}_y + v_z(x, y)\,\vec{e}_z$ is an arbitrary divergence-free field $\nabla \cdot \vec{v} = 0$, e.g. as is given in Eq. (16). The numerical solutions computed by our code for marginal cases of θ-pinch-like equilibria (see Fig. 5) showed the marginal behaviour described by (21).

3.3.3 Helical $\ell = 1$ equilibria without longitudinal current

Having studied numerically the stability of the θ-pinch, whose marginal characteristic is obscured by the $\ell = 4$ field and therefore shows the destabilizing effect of the δ_4-equilibrium distortion, we deal with $\ell = 1$ equilibria with a helical displacement of $\delta_1 = 1$ and a helical period number of $\varepsilon = 0.1$. Because the calculation is performed in a domain with a rotating square boundary, a small δ_4-distortion is inherent in the $\ell = 1$ equilibria. Since the $m = 2$, $ka = 0$ mode was of great interest for the discussion concerning the HBS project at Garching, we spent most of our effort on that particular mode. Some results are plotted in Fig. 6. Starting with rather coarse grids ($\Delta x = 1/6$), we always got stable results. But when we used a grid size of $\Delta x = 1/12$ or smaller, we got the unstable $m = 2$ mode. The plot shows the calculated eigenvalue γ^2 vs Δx for β values of $\beta = 0.5, 0.7, 0.9$.

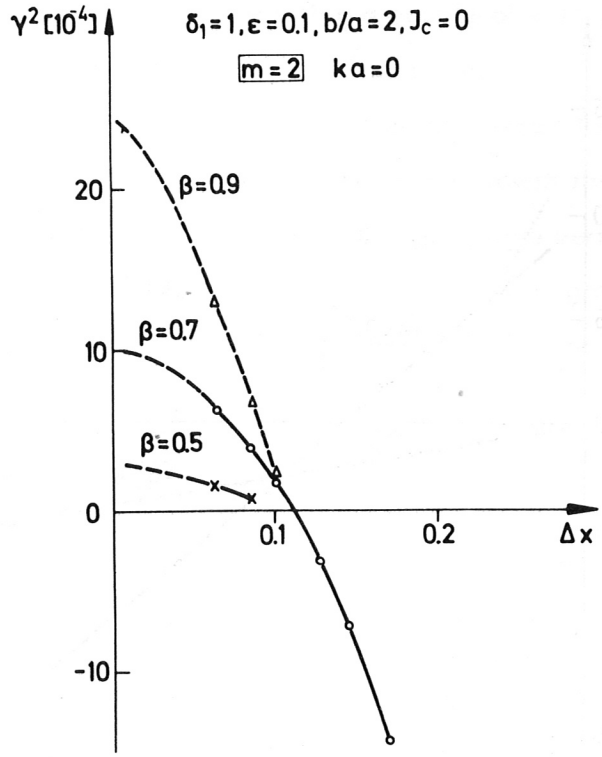

Fig. 6: Eigenvalue γ^2 vs Δx of m = 2, ka = 0 modes in helical $\ell = 1$ equilibria of different β values.

With increasing β, the slope $d\gamma^2/d(\Delta x)^2$ of the convergence curve γ^2 vs $(\Delta x)^2$ increases. The reason for that is that in the case of high-β values, the displacement of the helical magnetic axis with respect to the center of the outer boundary has become large (see Fig. 14), and hence the pressure gradient is large in the region where the flux surfaces are close together. Consequently, a smaller Δx is needed in order to describe sufficiently well the $\nabla \overset{\circ}{p}$ term in this region for high-β values.

In Fig. 7 the convergence curves γ^2 vs $(\Delta x)^2$ are plotted for different m (ka = 0) modes in equilibria without longitudinal net current. The m = 1 mode in a θ-pinch equilibrium shows a more favourable convergence behaviour than the more finely structured $m \geq 2$ modes in the $\ell = 1$ equilibrium.

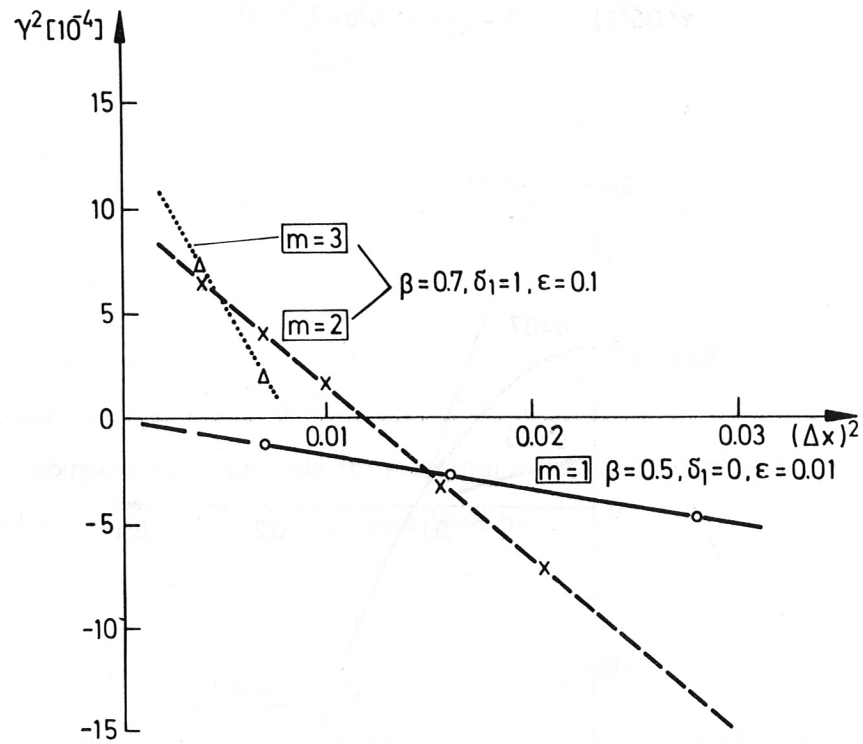

Fig. 7: Convergence behaviour of eigenvalue γ^2 of m = 1, 2, 3 modes with ka = 0 in equilibria with vanishing longitudinal net current (b/a = 2, J_c = 0).

The essence of these convergence tests is twofold: all these investigations were primarily intended to improve the reliability of the numerical results. On the other hand, this phenomenological picture of the influence of numerical dispersion and dissipation may give some hints for improving the approximation and the numerical scheme. Practically speaking, one could try to use higher-order approximations with all their specific problems or possibly try to use more appropriate coordinate systems. But up to now, we have used this code as it is in order to obtain some relevant physical results which are described in the next section.

4. Results

Because the rather high effort in computing a couple of e-folding times of the time evolution of the instability prevents a detailed parameter variation, we could only do a limited series of cases which are of particular interest for the HBS experiment at Garching. First, we give the dependence of the growth rate on the wave number k of the m = 2 instability. The resulting dispersion curve versus ka calculated for $\Delta x = 0.06$ is plotted in Fig. 8. The calculated maximum growth rate is near ka=0, but not exactly; the maximum value of γ is reached at ka $\doteq$ -0.015.

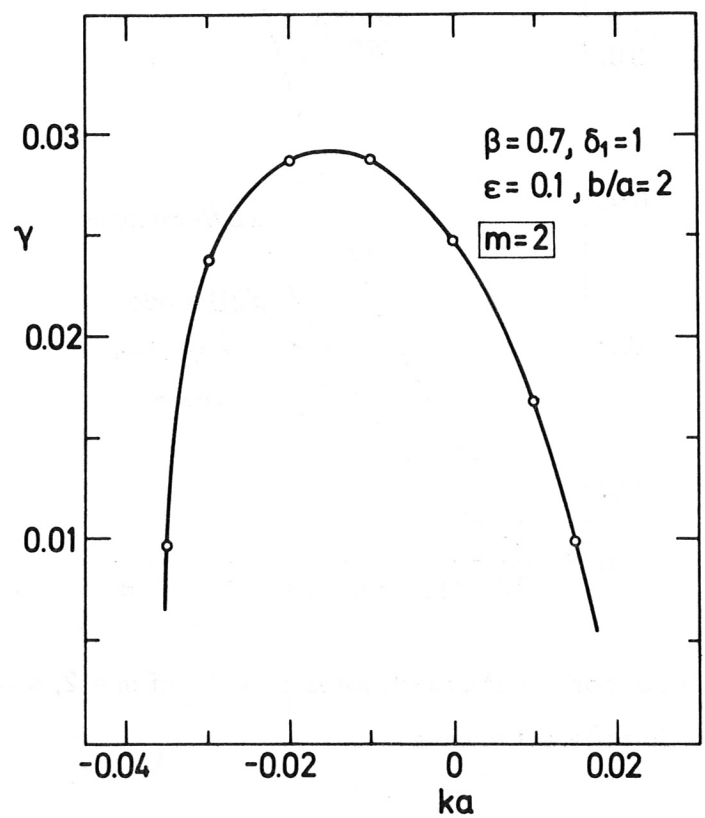

Fig. 8: Dispersion curve γ vs ka of the m = 2 mode in a helical $\ell = 1$ equilibrium ($\Delta x = 0.06$, $J_c = 0$).

The next variation is on β; in addition, this result is also important for the comparison with surface current theory / 4 / which predicts eigenvalues as given in Eqs. (22) - (24), and a δW analysis carried out for a diffuse pressure profile / 9 / by using a small ε expansion. It turned out that the solution of the initial-boundary-value problem

agrees very well with the latter and gives growth rates which are a factor of 2 smaller than those predicted by the surface current model. This is shown in Fig. 9. Besides the results obtained for $\Delta x = 0.06$, the extrapolated growth rates for $\Delta x \to 0$ are plotted, too.

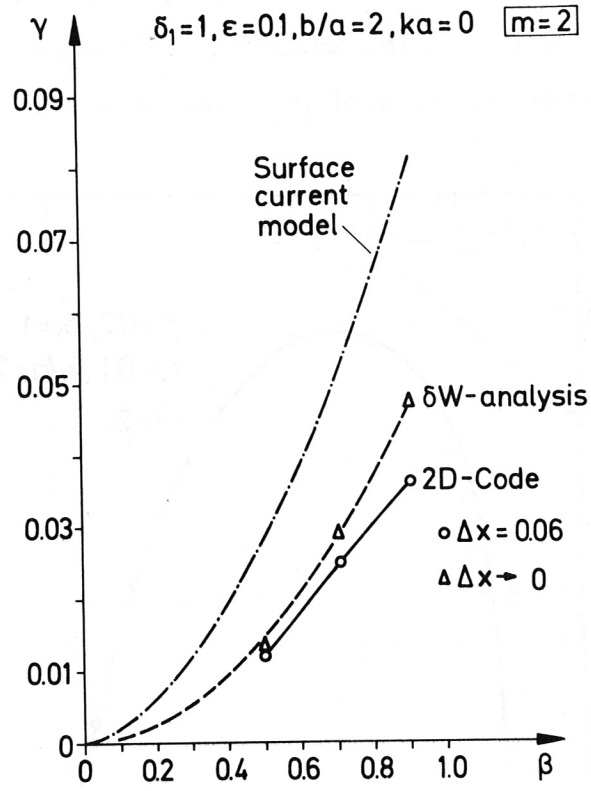

Fig. 9: Comparison of growth rates γ vs β of m = 2, k = 0 modes in different models.

The eigenvalues γ^2 obtained from the surface current model / 4 / read for $\delta_1 \ll \varepsilon < 1$:

$$\gamma^2 = \sum_{\ell} \beta (\delta_\ell \varepsilon \ell)^2 \, m \, (G1_{\ell m} + G2_{\ell m}), \tag{22}$$

$$G1_{\ell m} = \frac{1}{2(2-\beta)} \left\{ 4(1-\beta)(\ell-1) + \beta^2 (\max [m, \ell] - 1) \right\}, \tag{23}$$

$$G2_{\ell m} = \begin{cases} \dfrac{(2-\beta)(4-3\beta)\,\varepsilon^2}{(1-\beta)\,8} - \dfrac{\beta}{(b/a)^4}, & \text{for } \ell = 1, m = 1 \\ 0 & \text{for } \ell > 1, m > 1. \end{cases} \tag{24}$$

Another parameter variation is the increase of the helical displacement δ_1 of the plasma column. The growth rates of an m = 2, ka = 0 mode and of an m = 3, ka = 0 mode calcu-

lated for $\Delta x = 0.06$ are shown in Fig. 10 and Fig. 11. Again a comparison with other models is made, and again the code yields reduced growth rates.

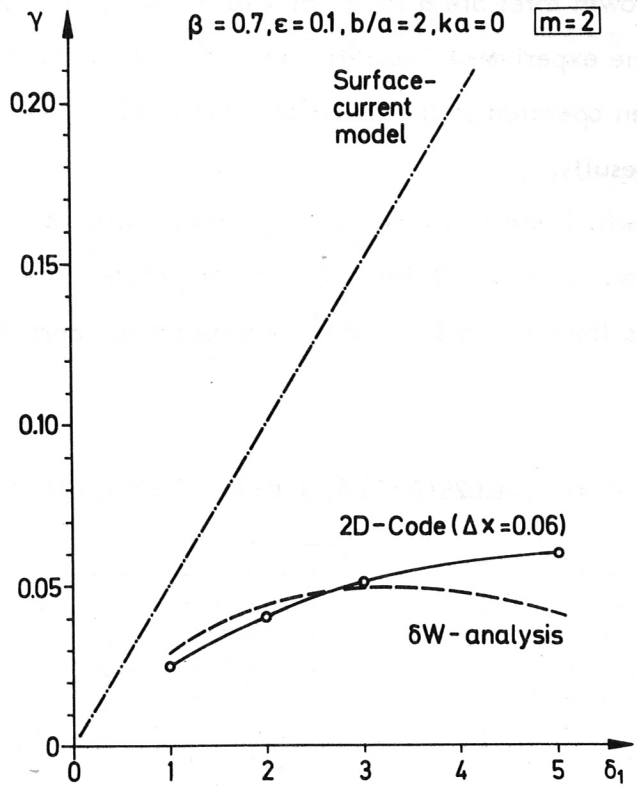

Fig. 10: Growth rate γ vs δ_1 of the m = 2, ka = 0 mode.

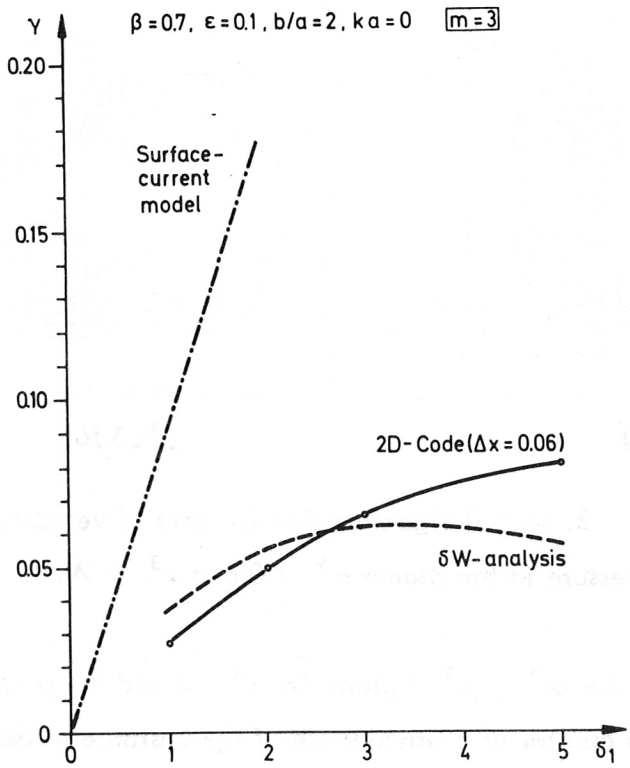

Fig. 11: Growth rate γ vs δ_1 of the m = 3, ka = 0 mode.

To summarize these quantitative results, one can say that within the parameter regime of interest ($\beta \simeq 0.5 \div 0.9$, $\delta_1 \simeq 1 \div 3$, $\varepsilon = 0.1$) the calculations are in good agreement with the δW results and the growth rates are a factor of 2 to 3 smaller than predicted by the surface current model. The experimental results obtained from the Garching ISAR T1-B experiment / 1 / when operated in the collision dominated regime also agree rather well with our numerical results.

To illustrate the eigenfunctions which are obtained by computation with $\Delta x = 0.06$ in a helical equilibrium, we selected an m = 2 (ka = 0) mode and plotted the velocity field in the (x^1, x^2) plane and the contour lines of the corresponding perturbed pressure (Fig. 12).

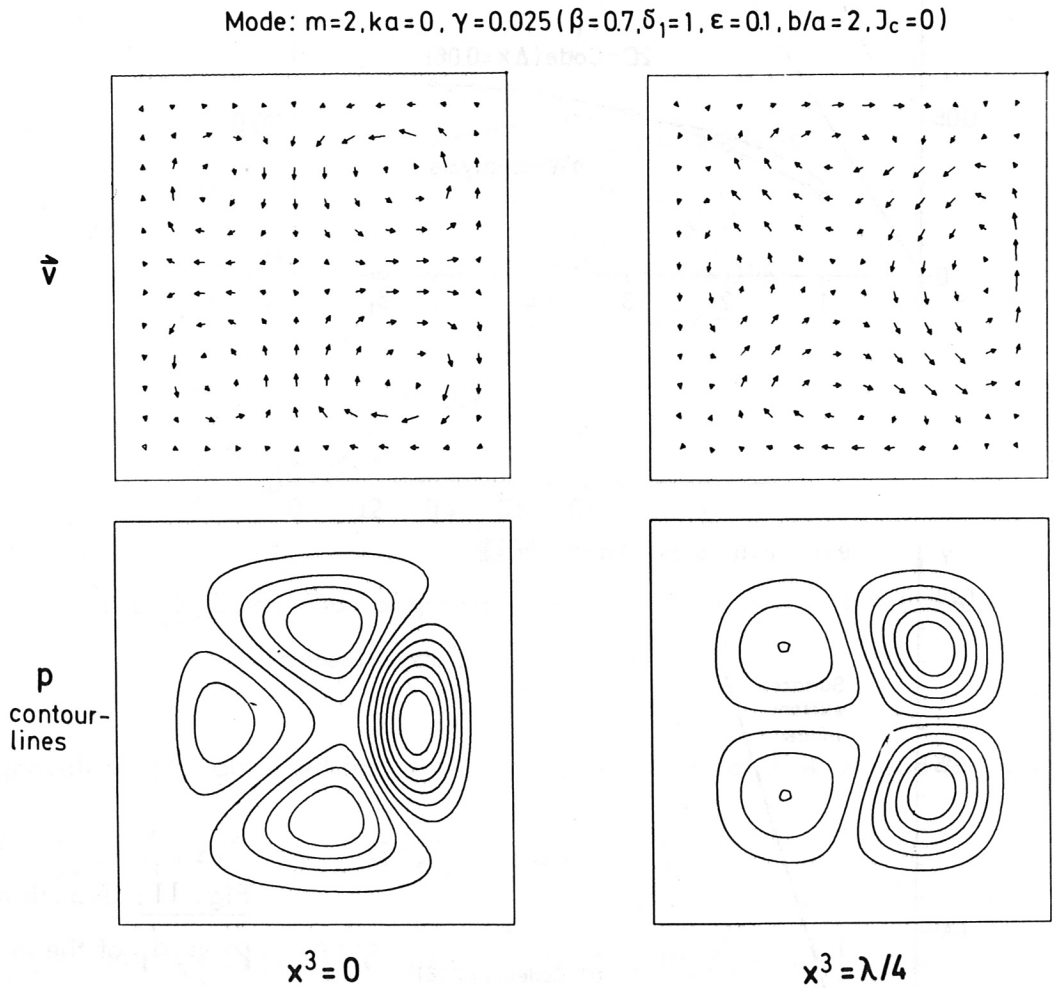

Fig. 12: The m = 2, ka = 0 eigenfunction in terms of velocity field and pressure in the planes $x^3 = 0$ and $x^3 = \lambda/4$.

The pictures on the left are in the (x^1, x^2) plane for $x^3 = 0$ and the pictures on the right are at $x^3 = \lambda/4$, i.e. a quarter of a wavelength of the unstable mode down the tube. This plot should illustrate the rotating feature of the instability in the rotating

coordinate system.

Fig. 13 likewise shows an m = 3 (ka = 0) mode in a helical $\ell = 1$ equilibrium.

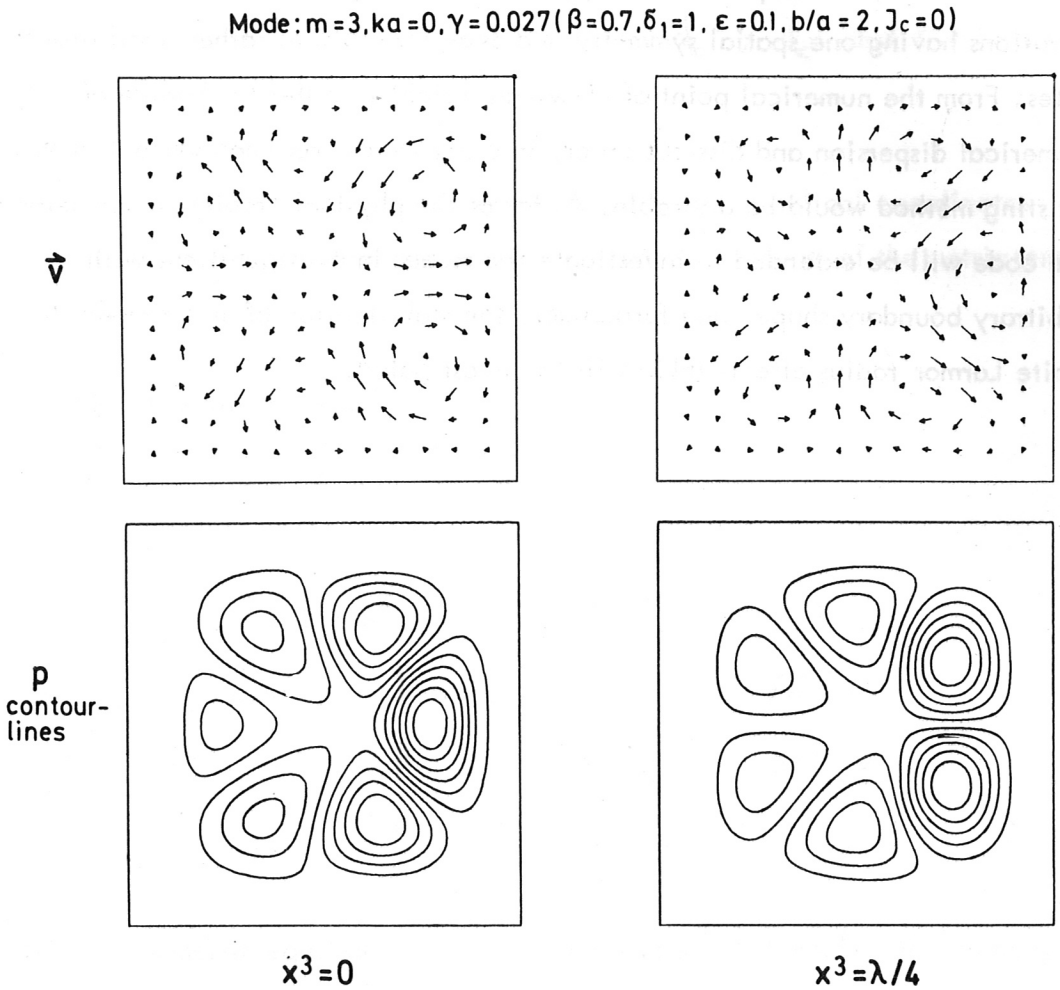

Fig. 13: The m = 3, ka = 0 eigenfunction in terms of velocity field and pressure in the planes $x^3 = 0$ and $x^3 = \lambda/4$.

5. Conclusions

The method of calculating the gross MHD instabilities by solving the linearized initial-boundary-value problem is applicable to arbitrary equilibrium configurations having one spatial symmetry and even for cases of rather small growth rates. From the numerical point of view, an insight into the mechanism of numerical dispersion and dissipation or, in other words, an improvement of the existing method would be desirable. As far as the physical problem is concerned, the code will be extended to investigate the modes in configurations with arbitrary boundary shape, and furthermore the stabilization of m = 2 modes by finite Larmor radius effects (FLR) will be investigated.

Appendix A: Coordinate System, Helical Equilibria

We use a non-orthogonal helical coordinate system (x^1, x^2, x^3) (see Fig. 1) which consists of cartesian coordinates (x^1, x^2) rotating around a helically deformed x^3 coordinate axis. The helical coordinate axis has the period length $L = 2\pi/h$ of the helical $\ell = 1$ field and a helix amplitude of $D_c = a\,\delta_c$; δ_c and $\epsilon = ha$ are normalized to the mean radius a of the plasma column.

The transformation of coordinates from cartesian (x, y, z) to helical coordinates (x^1, x^2, x^3), and the covariant and contravariant components of the metric tensor read:

$$x^1 = x \cos hz + y \sin hz - a\delta_c \,, \tag{A1}$$

$$x^2 = -x \sin hz + y \cos hz \,, \tag{A2}$$

$$x^3 = z \,, \tag{A3}$$

$$g_{11} = g_{22} = 1, \quad g_{33} = 1 + h^2 \left[(x^1 + a\delta_c)^2 + (x^2)^2 \right] \,, \tag{A4}$$

$$g_{12} = 0, \quad g_{13} = -hx^2 \,, \quad g_{23} = h(x^1 + a\delta_c), \quad \sqrt{g} = 1, \tag{A5}$$

$$g^{11} = 1 + (hx^2)^2 \,, \quad g^{22} = 1 + h^2 (x^1 + a\delta_c)^2 \,, \quad g^{33} = 1, \tag{A6}$$

$$g^{12} = -h^2 (x^1 + a\delta_c) x^2 \,, \quad g^{13} = hx^2 \,, \quad g^{23} = -h(x^1 + a\delta_c). \tag{A7}$$

The helically symmetric equilibria are independent of x^3 ($\partial/\partial x^3 = 0$) and obey the static MHD equations:

$$\nabla \overset{\circ}{p} = \overset{\circ}{\vec{J}} \times \overset{\circ}{\vec{B}}, \qquad \mu_0 \overset{\circ}{\vec{J}} = \nabla \times \overset{\circ}{\vec{B}}, \qquad \nabla \cdot \overset{\circ}{\vec{B}} = 0 \,. \tag{A8}$$

The solution of these equations is usually represented by a flux function ψ obeying the nonlinear elliptic differential equation:

$$\Delta^* \psi = \frac{2I}{(g_{33})^2} - \frac{1}{h^2}\left(\overset{\circ}{p}' + I I'/g_{33}\right) \,, \tag{A9}$$

$$\begin{aligned} g_{33} \Delta^* \psi = {} & \left[1 + (g^{13})^2\right] \psi_{,11} + \left[1 + (g^{23})^2\right] \psi_{,22} \\ & + h(1 + 2/g_{33})(g^{23}\psi_{,1} - g^{13}\psi_{,2}) + 2 g^{12} \psi_{,12} \,, \end{aligned} \tag{A10}$$

where $\overset{\circ}{p}(\psi)$ and $I(\psi)$ are arbitrary functions of ψ. For brevity, the derivatives are denoted by indices $,j := \partial/\partial x^j$ and $' := d/d\psi$. The magnetic field $\overset{\circ}{\vec{B}}$ and the current density $\overset{\circ}{\vec{J}}$ are then given by the covariant and contravariant components, respectively:

$$\overset{\circ}{B}{}^1 = -\frac{h}{\sqrt{g}}\,\psi_{,2}\,, \qquad \overset{\circ}{B}_1 = g_{11}\,\overset{\circ}{B}{}^1 + g_{13}\,\overset{\circ}{B}{}^3\,, \tag{A11}$$

$$\overset{\circ}{B}{}^2 = \frac{h}{\sqrt{g}}\,\psi_{,1}\,, \qquad \overset{\circ}{B}_2 = g_{22}\,\overset{\circ}{B}{}^2 + g_{23}\,\overset{\circ}{B}{}^3\,, \tag{A12}$$

$$\overset{\circ}{B}{}^3 = \frac{h}{\sqrt{g}\,g_{33}}\left[g^{23}\psi_{,1} - g^{13}\psi_{,2}\right] - \frac{g^{33}I}{g_{33}}\,, \qquad \overset{\circ}{B}_3 = -I(\psi)\,, \tag{A13}$$

$$\overset{\circ}{J}{}^1 = -\frac{I'}{\sqrt{g}}\,\psi_{,2}\,, \qquad \overset{\circ}{J}_1 = g_{11}\,\overset{\circ}{J}{}^1 + g_{13}\,\overset{\circ}{J}{}^3\,, \tag{A14}$$

$$\overset{\circ}{J}{}^2 = \frac{I'}{\sqrt{g}}\,\psi_{,1}\,, \qquad \overset{\circ}{J}_2 = g_{22}\,\overset{\circ}{J}{}^2 + g_{23}\,\overset{\circ}{J}{}^3\,, \tag{A15}$$

$$\overset{\circ}{J}{}^3 = \frac{1}{h\sqrt{g}}\left(-\overset{\circ}{p}{}' + B^3 I'\right)\,, \qquad \overset{\circ}{J}_3 = -\frac{1}{h}\left(g_{33}\,\overset{\circ}{p}{}' + I I'\right)\,. \tag{A16}$$

To solve Eq. (A9) numerically, we use a code by Marder /9/. The appropriate boundary conditions ($\vec{B}.\vec{n} = 0$) for an ideal electrically conducting wall are given at a square boundary of side length 2b. The geometric centre of the square is shifted by an amount of $D_1 = a\,\delta_1$ in the direction normal to the magnetic axis away from the origin of the coordinate system (see Fig. 1). The total normalized helical shift of the geometric centre of the square is given by $\delta = \delta_c + \delta_1$. In fact, without loss of generality, all calculations were carried out for $D_c = 0$ and hence $\delta = \delta_1$. The helical distortion δ_1 is somewhat different from the helical shift δ_{MA} of the magnetic axis where $\psi = 0$, but δ_1 is an adequate measure of the helical distortion of the plasma column for the comparison with the surface current constant pressure model (e.g. for $\varepsilon = 0.1$, $b/a = 2$, $\delta_1 = 1$: (a) $\beta = 0.5$, $\delta_{MA} = 1.23$; (b) $\beta = 0.9$, $\delta_{MA} = 1.54$).

The helical equilibria are characterized by the following five dimensionless parameters: the plasma beta $\beta = \overset{\circ}{p} / (\overset{\circ}{\vec{B}}{}^2/2\mu_0 + \overset{\circ}{p})$ at the magnetic axis, δ_1, ε, the compression ratio b/a, and J_c characterizing the longitudinal net current.

Equation (A9) has to be solved for an arbitrary pressure profile $\overset{o}{p}(\psi)$ and an arbitrary function $I(\psi)$. In fact, Eq. (A9) is solved /9/ for the case of

$$I = \left[1 - \beta \exp(-c\,\psi) \right]^{1/2} \tag{A17}$$

where the constant c is determined by the compression ratio b/a, which is the arbitrary input parameter ($I(\psi_{wall}) = 1$). From the additional constraint of vanishing longitudinal net current on each magnetic surface

$$\oint_{\psi = \text{const.}} J^3 \, ds = \oint_{\psi = \text{const.}} \frac{1}{R\sqrt{g}} \left(-\overset{o}{p}{}' + \overset{o}{B}{}^3 I' \right) ds = 0 \,, \tag{A18}$$

the pressure profile is determined as a function of ψ. The line element ds and the line integral are taken along the contour lines ψ = constant of the magnetic surfaces in the (x^1, x^2) plane. The numerical values of ψ are stored and used as input data for the stability code, where according to (A11) - (A16) the equilibrium fields are calculated on the + - grid. Examples of helical equilibrium solutions just described are shown in Fig. 14 in terms of contour lines ψ = constant in the (x^1, x^2) plane.

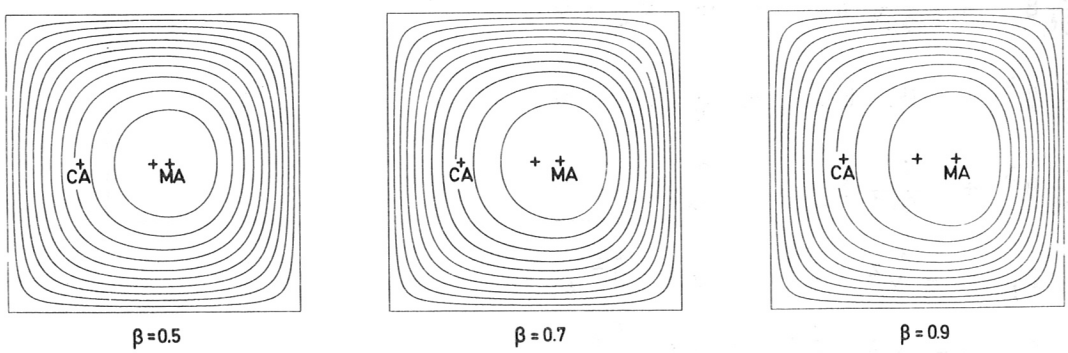

Fig. 14: Contour lines of flux surfaces of helical $\ell = 1$ equilibria for different β values (equilibrium parameters: $\delta_1 = 1$, $\epsilon = 0.1$, $b/a = 2$, $J_c = 0$; the coordinate axis and the magnetic axis are marked by CA and MA, respectively).

Appendix B: Linearized MHD Equations in a Helical Coordinate System

The system of partial differential equations for the perturbed quantities $\vec{v}$, p, and $\vec{B}$ is written in component form using covariant and contravariant vector notation ($i = \sqrt{-1}$):

$$\rho^{\circ} \frac{\partial}{\partial t} v^1 - g^{11} F_1 - g^{12} F_2 - g^{13} F_3 = 0 , \tag{B1}$$

$$\rho^{\circ} \frac{\partial}{\partial t} v^2 - g^{21} F_1 - g^{22} F_2 - g^{23} F_3 = 0 , \tag{B2}$$

$$\rho^{\circ} \frac{\partial}{\partial t} v^3 - g^{31} F_1 - g^{32} F_2 - g^{33} F_3 = 0 , \tag{B3}$$

$$F_1 = - \frac{\partial}{\partial x^1} p + \sqrt{g} \left(J^2 B^{\circ 3} - J^3 B^{\circ 2} + J^{\circ 2} B^3 - J^{\circ 3} B^2 \right) , \tag{B4}$$

$$F_2 = - \frac{\partial}{\partial x^2} p + \sqrt{g} \left(J^3 B^{\circ 1} - J^1 B^{\circ 3} + J^{\circ 3} B^1 - J^{\circ 1} B^3 \right) , \tag{B5}$$

$$F_3 = - iK\, p + \sqrt{g} \left(J^1 B^{\circ 2} - J^2 B^{\circ 1} + J^{\circ 1} B^2 - J^{\circ 2} B^1 \right) , \tag{B6}$$

$$\frac{\partial}{\partial t} p + v^1 \frac{\partial}{\partial x^1} p^{\circ} + v^2 \frac{\partial}{\partial x^2} p^{\circ} + \varkappa\, p^{\circ} \left[\frac{\partial}{\partial x^1} v^1 + \frac{\partial}{\partial x^2} v^2 + iK v^3 \right] = 0 , \tag{B7}$$

$$\frac{\partial}{\partial t} B^1 + \frac{\partial}{\partial x^2} E_3 - iK\, E_2 = 0 , \tag{B8}$$

$$\frac{\partial}{\partial t} B^2 + iK\, E_1 - \frac{\partial}{\partial x^1} E_3 = 0 , \tag{B9}$$

$$\frac{\partial}{\partial t} B^3 + \frac{\partial}{\partial x^1} E_2 - \frac{\partial}{\partial x^2} E_1 = 0 , \tag{B10}$$

$$E_1 = - v^2 B^{\circ 3} + v^3 B^{\circ 2} , \tag{B11}$$

$$E_2 = - v^3 B^{\circ 1} + v^1 B^{\circ 3} , \tag{B12}$$

$$E_3 = - v^1 B^{\circ 2} + v^2 B^{\circ 1} , \tag{B13}$$

$$J^1 = \frac{\partial}{\partial x^2} B_3 - iK\, B_2 , \tag{B14}$$

$$J^2 = iK\, B_1 - \frac{\partial}{\partial x^1} B_3 , \tag{B15}$$

$$J^3 = \frac{\partial}{\partial x^1} B_2 - \frac{\partial}{\partial x^2} B_1 . \tag{B16}$$

Appendix C: Calculation Mesh

The equilibrium quantities $\overset{0}{Y} = \{ \overset{0}{p}, \overset{0}{B}, \overset{0}{\rho} \}$ are stored as REAL * 4 variables; all perturbed quantities $\overset{1}{Y} = \{ \vec{v}, p, \vec{B} \}$ are represented by COMPLEX variables and complex arithmetic is used for their calculation. The variables are defined on a staggered 2D (x^1, x^2) grid as follows:

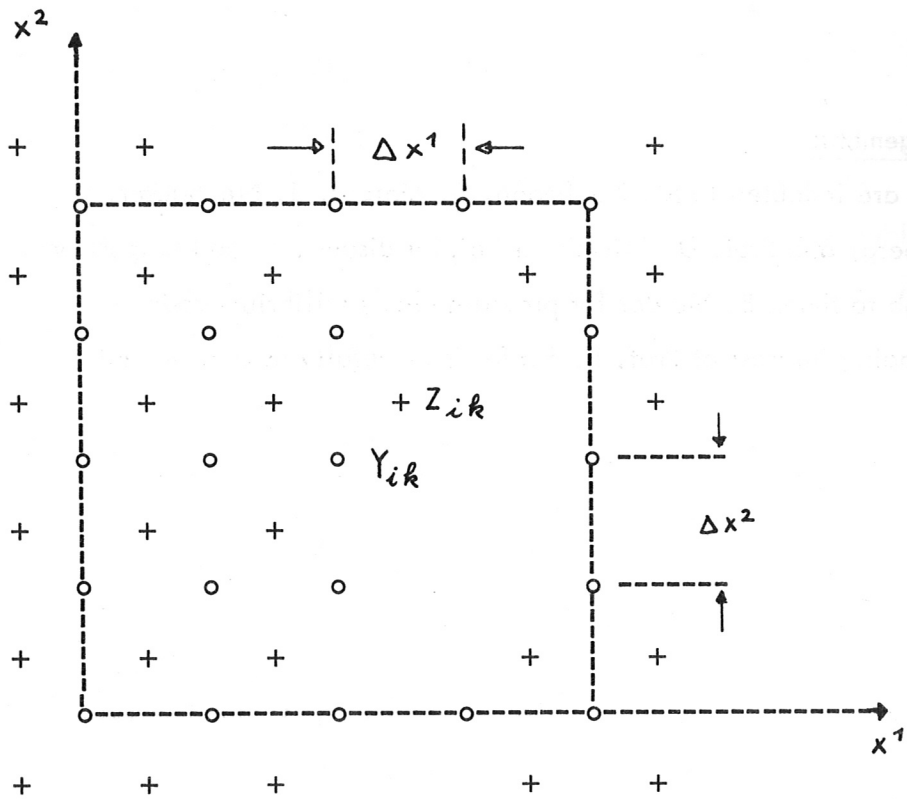

Fig. 15: Calculation grid.

On the grid denoted by o, the perturbed pressure and the perturbed magnetic field are defined:

"o" - grid: $Y_{ik} = \{ p, B^1, B^2, B^3 ; B_1, B_2, B_3 \}$.

On the grid denoted by +, all the equilibrium quantities $\overset{\circ}{Y}$ and the perturbed velocity components v^i are defined:

"+" - grid:

$$Z_{ik} = \begin{Bmatrix} \overset{\circ}{\rho} & \overset{\circ}{p}, & & v^1, & v^2, & v^3, \\ \overset{\circ}{B}^1, & \overset{\circ}{B}^2, & \overset{\circ}{B}^3, & E_1, & E_2, & E_3, \\ \overset{\circ}{J}^1, & \overset{\circ}{J}^2, & \overset{\circ}{J}^3, & J^1, & J^2, & J^3. \end{Bmatrix}$$

Acknowledgements

The authors are indebted to M. Kaufmann, B. Marder, J. Neuhauser, J. Nührenberg, and Prof. D. Pfirsch for helpful discussions and suggestions. We also wish to thank B. Marder for providing his equilibrium code. The encouraging interest of Prof. E. Fünfer is gratefully acknowledged.

References

/1/ Fünfer E., Kaufmann M., Neuhauser J., Schramm G., 7th Eur. Conf. Fusion and Plasma Physics, vol. 2, p. 151 (1975).

/2/ Davidson R.C., Freidberg J.P., 3rd Top. Conf. Pulsed High Beta Plasmas, (Culham, Sept. 1975); Preprint 601 Po21.

/3/ Braun W. et al., Plasma Physics and Controlled Nucl.Fus.Res. 1974 Vol. 3, p. 25, IAEA, Vienna (1975).

/4/ Rosenbluth M.N., Johnson J.L., Greene J.M., Weimer K.E., Phys. Fluids 12 (1969) 726.

/5/ Grad H., Weitzner H., Phys. Fluids 12 (1969) 1725.

/6/ Weitzner H., Phys. Fluids 14 (1971) 658.

/7/ Berge G., Freidberg J.P., Phys. Fluids 18 (1975) 1362.

/8/ Herrnegger F., Nührenberg J., Nucl. Fus. 15 (1975) 1025.

/9/ Marder B., Straight $\ell = 1$ Equilibrium and Stability, to be published.

/10/ Rosenbluth M.N., Krall N.A., Rostoker N., Nucl.Fusion Supl. Pt. 1 (1962) 143.

/11/ Freidberg J.P., Phys. Fluids 15 (1972) 1102.

/12/ Grimm R.C., Greene J.M., Johnson J.L., Meth. Comp. Phys. 16, Chap. 4, Academic Press, New York, 1976.

/13/ Kerner W., Tasso H., Plasma Phys. Contr. Nucl. Fusion Res., Vol. 1, p. 475, IAEA, Vienna 1975.

/14/ Freidberg J.P., Marder B.M., Phys. Fluids 16 (1973) 247.

/15/ Appert K., Berger D., Gruber R., Troyon F., Rappaz J., Z.Angew. Math. Phys. 25 (1974) 229.

/16/ Takeda T., Shimomura Y., Ohta M., Yoshikawa M., Phys. Fluids 15 (1972) 2193.

/17/ Sykes A., Wesson J.A., Nucl.Fusion 14 (1974) 645.

/18/ Bateman G., Schneider W., Grossmann W., Nucl.Fusion 14 (1974) 669.

/19/ Dibiase J.A., Killeen J., Robinson D.C., Schnack D., 3rd Top.Conf. Pulsed High-Beta Plasmas, (Culham, Sep. 1975).

/20/ Gerlakh N.I., Zueva N.M., Solove'v L.S., Preprint Nr. 96 (1975), Nr. 111 (1975), Moscow.

/21/ Rosenbluth M.N., Waddell B., Monticello D., White R., 7th Eur. Conf. Contr. Fusion and Plasma Physics, Vol. 2 (1975) 286, (Lausanne 1975).

/22/ Schwenn U., 2nd Eur. Conf. Comp. Phys., p. F1, IPP 6/147 (D. Biskamp, Ed., Garching 1976).

/23/ Lui H.C., Chu C.K., Phys. Fluids 18 (1975) 1277.

/24/ Brackbill J.U., Meth. Comp. Phys. 16, Chap. 1, Academic Press, New York, 1976.

/25/ Wooten J.W., Hicks H.R., Bateman G., Dory R.A., ORNL-TM 4784 (1974).

/26/ Chodura R., Schlüter A., 3rd Top. Conf. Pulsed High Beta Plasmas, (Culham, Sept. 1975).

/27/ Strauss H.R., Phys. Fluids 19 (1976) 134.

/28/ Herrnegger F., Schneider W., 7th Eur. Conf. Contr. Fusion and Plasma Physics, vol. 1, 109 (Lausanne 1975).

/29/ Herrnegger F., Schneider W., 2nd Eur. Conf. Comp. Phys., p. C5, (D. Biskamp, Ed., Garching 1976).